High-Sensitivity p–n Junction Photodiodes Based on PbS Nanocrystal Quantum Dots

*Bhola N. Pal, Istvan Robel, Aditya Mohite, Rawiwan Laocharoensuk, Donald J. Werder, and Victor I. Klimov**

Chemically synthesized nanocrystal quantum dots (NQDs) are promising materials for applications in solution-processable optoelectronic devices such as light emitting diodes, photodetectors, and solar cells. Here, we fabricate and study two types of p-n junction photodiodes in which the photoactive p-layer is made from PbS NQDs while the transparent n-layer is fabricated from wide bandgap oxides (ZnO or TiO_2). By using a p–n junction architecture we are able to significantly reduce the dark current compared to earlier Schottky junction devices without reducing external quantum efficiency (EQE), which reaches values of up to ~80%. The use of this device architecture also allows us to significantly reduce noise and obtain high detectivity (>10^{12} cm $Hz^{1/2}$ W^{-1}) extending to the near infrared past 1 μm. We observe that the spectral shape of the photoresponse exhibits a significant dependence on applied bias, and specifically, the EQE sharply increases around 500–600 nm at reverse biases greater than 1 V. We attribute this behavior to a "turn-on" of an additional contribution to the photocurrent due to electrons excited to the conduction band from the occupied mid-gap states.

1. Introduction

The capability to detect visible and infrared (IR) light with high sensitivity and high response speed is important in the fields of optical fiber communication,[1] medical diagnostics,[2] remote sensing, and digital imaging.[3,4] Solution-processable nanocrystal quantum dots (NQDs) are promising materials for the next generation of photodetectors. Due to the quantum size effect, their spectral response can be tuned by simply changing particle dimensions. Additionally, these structures offer the possibility for facile incorporation into devices using low-cost solution-based methods that are also compatible with flexible electronics.[5–7]

Recently, significant progress has been made in solution-processed NQD-based photodetectors using both photodiode[8–10] and photoconductor[11–13] configurations. However, by the standards of traditional bulk-semiconductor based optoelectronics, the operational parameters of these prototype structures still require improvements. Two specific challenges are the increase in the response speed and the detectivity. For the purpose of the improved speed, a photodiode configuration is prefererential to a photoconductor.[14] However, a typical drawback of NQD-based photodiodes is a high dark current,[9,10] which leads to a high noise level and thus limits the detectivity of the device. This is an especially serious problem with the Schottky-junction devices that have been most extensively explored in the case of NQD detectors. A p–n junction architecture is advantageous when compared to a Schottky junction due to reduced dark current and improved resistance under reverse bias, which should lead to improved detectivity. Recent works have demonstrated promising possibility for the use of NQD p–n junctions in solar cells.[15,16] However, so far this architecture has not been applied for realizing high-sensitivity photodetection.

Here, we demonstrate NQD p–n photodiodes of two different architectures that utilize p-doped nanocrystal films and n-type layers of solution-processed ZnO and TiO_2. In these devices, narrow-gap NQDs serve as an active light absorbing material, while wide-gap oxide semiconductors are used as charge transport materials. All stages of device manufacturing, except for deposition of electrodes, rely on routine low-temperature, wet-chemistry techniques that are easily scalable and readily applicable to large-area structures. Despite the relative simplicity of fabrication, the photodiodes exhibit strong performance, comparable to that of earlier reported NQD-photodiodes. Specifically, they feature a low dark current of 70–80 nA/cm^2 at room temperature and high detectivity of greater than 10^{12} cm $Hz^{1/2}W^{-1}$ extending from the visible to near-IR spectral energies. If excited with short laser pulses, they show a fairly fast response with a build up time of ~100 ns and a decay constant of a few μs. At low reverse biases, the photoconduction in these devices is dominated by photogenerated band-edge holes that are longer lived compared to electrons.

B. N. Pal, I. Robel, D. J. Werder
Center for Advanced Solar Photophysics
Chemistry Division
Los Alamos National Laboratory
Los Alamos, NM 87545, USA
A. Mohite, R. Laocharoensuk
Center for Integrated Nanotechnologies
Los Alamos National Laboratory
Los Alamos, NM 87545, USA
Dr. V. I. Klimov
Center for Advanced Solar Photophysics
Chemistry Division
Los Alamos National Laboratory
Los Alamos, NM 87545, USA
E-mail: klimov@lanl.gov

DOI: 10.1002/adfm.201102532

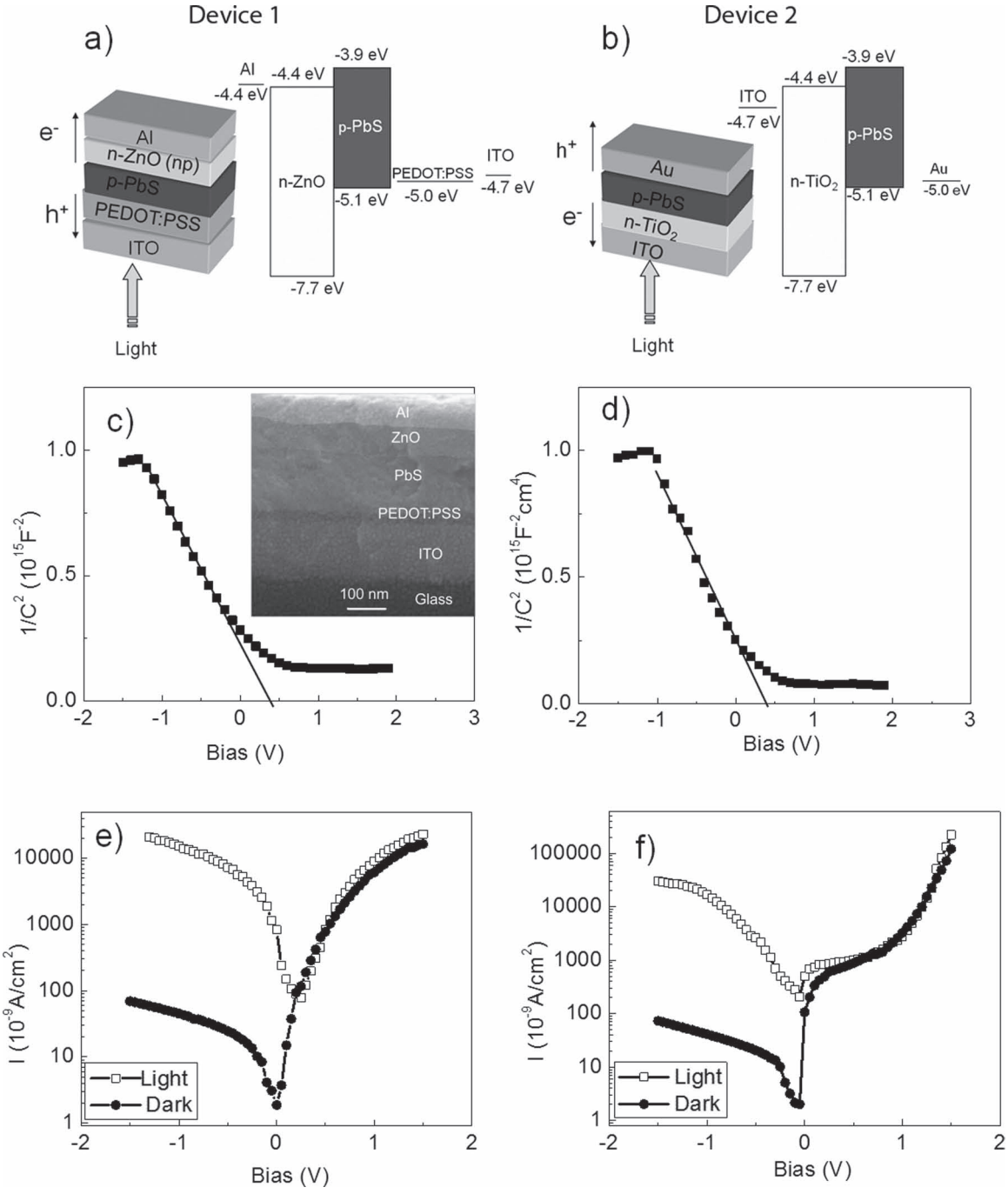

Figure 1. Device architectures along with energy level diagrams for a) ITO/PEDOT:PSS/PbS-NQD/ZnO/Al and b) ITO/TiO_2/PbS-NQD/Au photodiodes. c) Capacitance as a function of bias (*C–V* characteristics) for device 1. Inset: A cross-sectional structure of device 1 imaged using a scanning electron microscope. d) The *C–V* characteristic of device 2. e) The current–voltage (*I–V*) characteristics of device 1 in dark (solid circles) and under illumination (open squares) with 500 nm monochromatic light with intensity 200 μW cm^{-2}. f) The same for device 2.

However, at bias above ~1 V the carrier drift time becomes sufficiently short to allow for collection of photogenerated electrons, which leads to a sharp increase in the photocurrent. This is accompanied by a change in the spectral shape of the photoresponse, which can be explained by the involvement of transitions from extrinsic, likely surface related mid-gap states to intrinsic conduction band, quantized levels.

2. Results and Discussions

In **Figure 1**a and b, we show schematically two types of p–n junction devices studied in this work. In device 1 (Figure 1a), a p–n junction is formed at the interface between layers of p-type PbS NQDs and n-type ZnO nanoparticles. We also use PEDOT:PSS as an electron blocking layer, which helps us to

reduce dark current under reverse bias. The structure is completed with a bottom indium tin oxide (ITO) and a top Al contact. Device 2 (Figure 1b) is an inverted structure where a p-type NQD layer is assembled on top of an n-type TiO_2 film fabricated by a sol-gel process. TiO_2 is a wide-gap semiconductor and does not block visible light when the device is illuminated from the bottom ITO side (Figure 1b). In both devices the thickness of the NQD layer is ~150 nm. The mean diameter of the NQDs used in this study is 4 nm and the size polydispersity is ~9%. The NQD bandgap energy is 1.18 eV, as inferred from the position of the lowest energy 1S absorption feature of solution samples. The integrity and the size of the dots have been preserved following their incorporation into the devices. Specifically, the energy of the band-edge feature in the spectrally resolved photocurrent of the photodiodes (see below) is close to that of the 1S absorption peak in NQD solutions.

As we show below, for both structures, the nanocrystal layer is fully depleted and photogenerated electrons and holes are efficiently separated by the built-in field and collected at the electrodes. Based on the band-edge energy offsets, the oxide and the PbS NQDs layers form a type-II heterojunction (see Figure 1a and b). As a result, in addition to the built-in field, an "intrinsic" energy gradient at the type-II interface facilitates spatial separation of electrons and holes.

To characterize a p–n junction in these devices, and specifically, to determine the thickness of the depletion layer, we use capacitance-voltage (C–V) measurements. In Figure 1c, we show the C–V characteristics of device 1 plotted as $1/C^2$ vs. V. To analyze it, we assume that the doping level in the oxide material is much higher than in the nanocrystal film,[15] and therefore, the depletion region resides almost entirely within the NQD layer. In this case, one can apply the following expression for analyzing the C–V data:[14]

$$\frac{1}{C^2} = \frac{2}{q\,\varepsilon_s}\frac{(\phi - V)}{N_a} \tag{1}$$

where N_a is the acceptor concentration in the p layer, φ is the built-in potential, q is the electron charge, and ε_s is the effective dielectric constant of the NQD film. From the projected intersection of the measured $1/C^2$ dependence with the horizontal axis, we find φ of ~0.5 V. From the slope of this dependence, we further obtain that N_a is ~2×10^{16} cm^{-3} (calculated using ε_s = 15[17]). Using these data, we can now calculate the width (W) of the depletion layer from the expression:[14]

$$W = \sqrt{\frac{2\varepsilon_s(\phi - V)}{q\,N_a}} \tag{2}$$

For device 1, this expression yields W of ~190 nm (at 0 V). A comparable depletion width is also obtained from the C–V measurements of device 2 (Figure 1d). These results indicate that in our structures the depletion region extends across the entire thickness of the NQD layer (~150 nm) even at zero bias.

The significant thickness of the depletion layer together with a large type-II band-edge offset are expected to lead to a considerable suppression of dark current (I_d) under reverse bias. Indeed, the current-voltage (I–V) characteristic of these structures (Figure 1e and f) indicate I_d of only ~80 nA cm^{-2} at V = –1.5 V. This is two orders of magnitude lower than in previously reported NQD-based Schottky photodiodes.[9,10] Our devices also show a strong rectifying behavior in dark with a rectification ratio of ~10^3 at ±1.5 V (see Figure 1e and f). This is another signature of a well-insulating junction at the interface between the p and n layers.

In addition to low dark current these structures show a strong photoresponse as illustrated by the I–V measurements under monochromatic illumination (wavelength λ = 500 nm) shown in Figure 1e and f. For incident light intensity of 200 μW cm^{-2} we measure photocurrent of ~27 μA cm^{-2} (V = –1.5 V), which translates into a fairly high external quantum efficiency (EQE) of 34%. Further, the ratio of the photocurrent to dark current is also quite high, being greater than 150. This initial characterization suggests that these structures can perform strongly as high sensitivity detectors.

A key figure of merit of a photodiode is the noise equivalent power (NEP). This parameter is defined as the amount of incident light power, which generates a photocurrent equal to the noise current. NEP can be expressed as:[14,18]

$$NEP = \frac{\sqrt{\langle I_n^2 \rangle}}{R} \tag{3}$$

where $\langle I^2_n \rangle$ is the time-averaged square of the total noise current and R is the responsivity, which is the ratio of the photocurrent to the incident light power. The responsivity can be directly inferred from the EQE measurements using the expression: $R = 0.806\lambda \times$ EQE, where λ is the wavelength measured in μm; this yields R in units of A/W. Another parameter widely used to characterize the performance of photodiodes is the detectivity (D^*), which is related to NEP by the following expression:[14,18]

$$D^* = \frac{\sqrt{A\Delta f}}{NEP} \tag{4}$$

where A is the photosensitive area of the device and Δf is the detection bandwidth.

To characterize our devices in terms of the above characteristics, we have conducted the studies of spectrally resolved EQE and noise currents. **Figure 2**a and b show the measured EQE as a function of λ for different applied biases for devices 1 and 2, respectively. In both cases, the magnitude of the EQE increases with V; however, this increase is not linear, but exhibits a sharp onset at around 1–1.25 V, which is especially pronounced in device 1 (see plots of EQE vs. V in Figure 2c and d). Further, the EQE growth is not spectrally uniform and peaks around ~500–600 nm.

These peculiarities in the V-dependence of EQE can be explained using a recent study of charge transport and photoconduction in p-doped PbS NQD films incorporated into optical field effect transistors.[19] This study shows that photoconduction in these films is strongly affected by intra-gap states that form a weakly conducting mid-gap band (MGB). As was pointed out previously,[19] the development of MGB conductance was observed only following the treatment of NQD films with molecules of ethanedithiol, the procedure also used in the present study (see Experimental Section). Since this treatment does not affect NQD sizes (the position of the band-edge peak does not appreciably change following the treatment), it likely

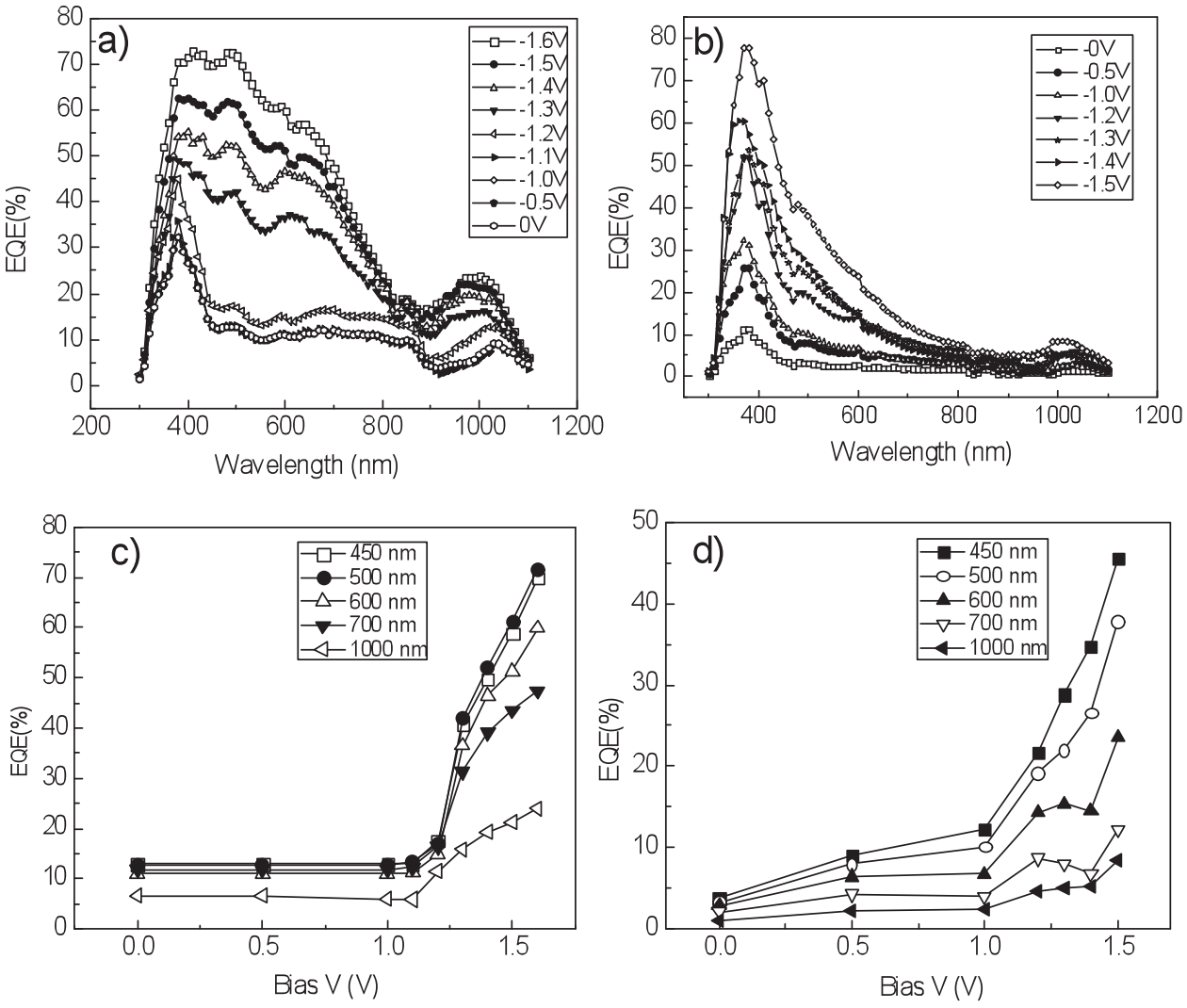

Figure 2. External quantum efficiency (EQE) at different biases as a function of wavelength for a) device 1 and b) device 2. EQE at different wavelengths as a function of reverse bias for c) device 1 and d) device 2.

modifies only the properties of the NQD surfaces. This suggests that the MGB states are surface-related.

The role of the MGB is two-fold. First, its occupancy defines carrier lifetimes as the dynamics of the mobile band-edge charges are controlled by trapping at the MGB states. Further, this band optically couples to quantized states, which leads to the development of new optical transitions in both intra-gap and above-gap regions.[19] Based on the gate-voltage dependence of photoconduction, a previous study[19] concluded that the trapping rate for electrons is much greater than for holes. As a result, photoconduction is dominated by valence-band holes as their lifetime, τ_h, is considerably longer than that of electrons, τ_e. The mobile holes in these films can be generated via both the band-to-band transitions and the valence-band-to-MGB transitions (see **Figure 3**a). However, in the case of a nearly fully occupied MGB, which is the case in non-gated films studied here,[19] the role of the latter transition is insignificant because of Pauli blocking. On the other hand, the role of MGB–to-conduction-band transitions is increased. These transitions, though, are difficult to observe in the photocurrent because of a short trapping time of the band-edge electrons. In order to see the contribution from these transitions to photocurrent, the extraction time of electrons from the NQD layer must be shorter than their lifetime; this can be accomplished by increasing the built-in field in the p–n junction and/or increasing reverse bias on device terminals.

Given the scenario of photoconduction outlined above, we can propose the following explanation for the observed EQE vs. *V* dependence. In our fully depleted NQD films, the transport is primarily due to drift of photogenerated charges. Under zero bias, the drift time t_d is shorter than the hole lifetime but longer than the electron lifetime: $\tau_e < t_d < \tau_h$ (see schematics in Figure 3b). In this case, photogenerated electrons are trapped at mid-gap states before they are extracted into the n-type layer and the photocurrent is almost exclusively due to holes (the conductivity of MGB, which serves as a conduit for transport

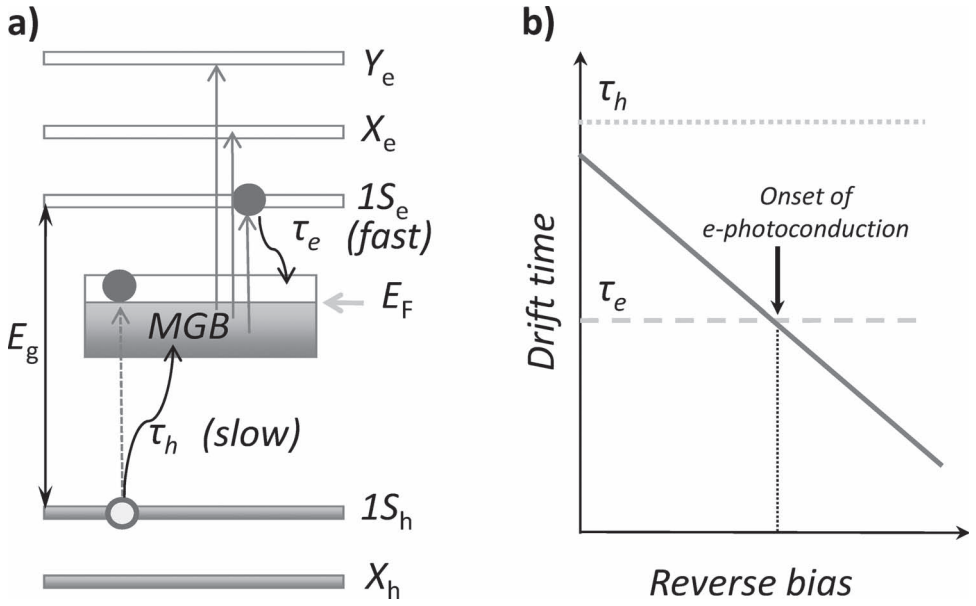

Figure 3. a) Schematic diagram illustrating optical transitions and relaxation channels involving the NQD quantized states (1S, X, and Y; subscripts "e" and "h" label the states in the conduction and the valence band, respectively) and the states of the mid-gap band (MGB); see text for details. b) Schematic illustration of the dependence of the electron drift time on reverse bias relative to the electron and hole lifetimes. The vertical arrow indicates the onset of the contribution from photogenerated electrons to the photocurrent.

of trapped electrons, is much smaller than that of the valence band-edge states[19]).

As the bias is increased, the drift time decreases until it eventually becomes shorter than τ_e (Figure 3b). This defines the onset of electron contribution to photoconduction, which is manifested in our experiments as a sharp increase in the photocurrent (Figure 2c and d). The increased contribution from the electrons should be especially pronounced in the spectral region of the MGB-to-conduction-band transitions, as these transitions while exciting the electrons into extended quantized states do *not* generate mobile holes. The transition from the MGB to the lowest energy $1S_e$ conduction-band level (see Figure 3a) is in the intra-gap region, and it is not observed in our experiments because of the limited spectral range of our measurements on the IR side of the spectrum. However, the transitions from the MGB to the higher energy conduction-band states (labeled, $1X_e$ and $1Y_e$ in Figure 3a) may correspond to above-gap energies, which can explain a spectrally selective enhancement in the photocurrent at wavelengths shorter than 800 nm observed here. The spectrally resolved studies of photoconductance in PbS NQD films performed in ref. 19 indeed indicate that in addition to the sub-gap features, MGB can also produce features at above-gap energies.

The proposed mechanism of photoconduction also explains a higher sensitivity of a photoresponse to applied bias in device 1 compared to device 2. Given the structure of device 1 (see Figure 1a) and the fact that it is illuminated from the bottom ITO side, charge photogeneration occurs primarily near the PbS NQD–PEDOT:PSS interface. Therefore, in order to be extracted, the electrons must travel through the entire thickness of the nanocrystal layer. On the other hand, in device 2 (Figure 1b), the electrons are generated immediately next to the electron-transporting TiO_2 layer. Therefore, the electron drift time in device 2 on average is shorter than that in device 1 and as a result, the onset for electron photoconduction should occur at a lower bias. This is indeed observed experimentally (compare Figure 2a and b).

The increasing contribution from the MGB-related transitions under increasing bias has an important implication for the spectral shape of the photoresponse in these devices. At low biases it mimics the linear absorption of solution samples and fairly quickly drops from the blue to the IR part of the spectrum. On the other hand, as the bias is increased the photoresponse becomes more spectrally uniform, which is due to increasing contribution from the MGB-to-conduction-band transitions discussed above. As a result of this increase, the high EQE values of more than 50% are maintained across a wide range of wavelengths from ~350 to ~700 nm (device 1; $V = -1.6$ V). Even at 1 μm the EQE is still high, ~20%.

According to Equations (3) and (4), in addition to large EQE, high detectivity requires a low level of noise. The ultimate limit of noise in photodetectors is defined by shot noise, which arises from statistical nature of the current (it is due to migration of discrete charges). The shot noise can be expressed as $\langle I^2_{sn}\rangle = 2e(I_{ph} + I_d)\Delta f$, where I_{ph} is the photocurrent.[14] At low light intensities used to determine ultimate sensitivity of devices, one can consider only a dark current contribution to I_{sn}. Based on dark current measurements of our photodiodes (Figure 1e and f), $I_d = 7.2$ nA (device area is 0.09 cm^2) at $V = -1.5$ V, which yields the shot noise spectral density of ca. 0.002 pA^2 Hz^{-1} (defined in terms of $\langle I^2_{sn}\rangle/\Delta f$). In **Figure 4**a, we compare this value with results of direct dark noise measurements conducted under the –1.5 V bias. For both types of devices the noise spectrum shows a fast fall-off with increasing f as it approaches the shot-noise limit (horizontal line in Figure 4a). Based on the measurement for device 1, the total noise current within the

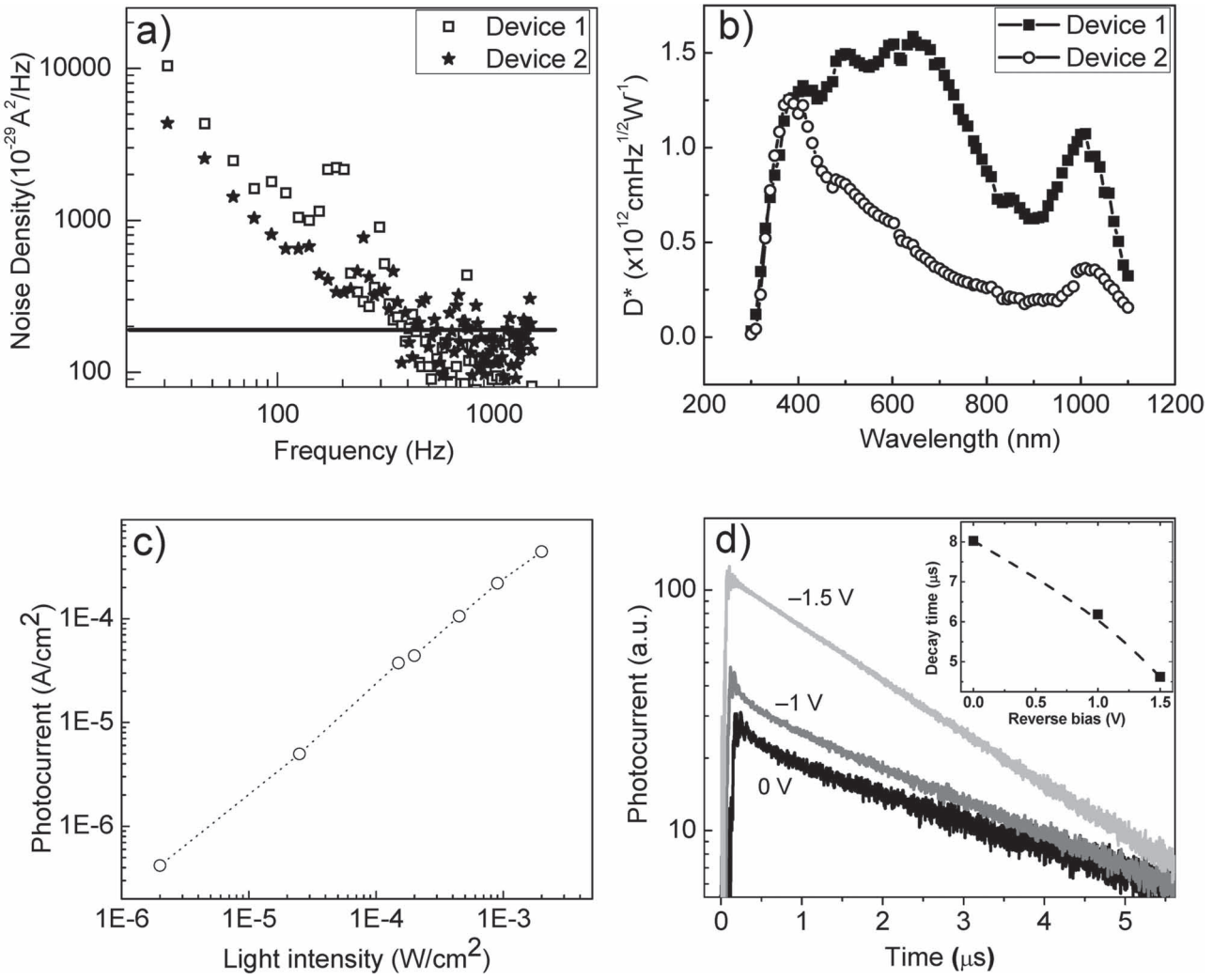

Figure 4. a) Dark current noise density under reverse bias of 1.5 V as a function of frequency (open square device 1, solid star device 2); horizontal line is the shot noise limit. b) Detectivity spectra under the –1.5 V reverse bias as a function of wavelength for device 1 (solid squares) and 2 (open circles). c) Photocurrent as a function of light intensity under –1.5 V reverse bias for device 1 (500 nm illumination). d) Transient photocurrent for device 1 under different biases excited by femtosecond laser pulses at 800 nm. Inset: Photocurrent decay time as a function of reverse bias.

1.5 kHz bandwidth is ~2.3 pA, which corresponds to NEP of ~9 pW at 500 nm. This value is close to that for the shot-noise limit (~7 pW) indicating that in our devices I_n is indeed dominated by shot noise and hence is directly linked to dark current. Therefore, the architecture of our photodiodes designed to reduce I_d is well suited for realizing low-noise, and hence, high-detectivity devices.

Using the EQE spectrum obtained for the –1.5 V bias (Figure 2a and b) and the measured noise current (Figure 4a), we calculate the detectivity of our devices, which is shown in Figure 4b. For device 1, D^* peaks is at ~700 nm where it reaches the value of 1.45×10^{12} cm $Hz^{1/2}$ W^{-1}. Due to a fairly "flat" EQE spectrum, the detectivity remains high on both the blue (1.3×10^{12} cm $Hz^{1/2}$ W^{-1} at 400 nm) and IR (1.1×10^{12} cm $Hz^{1/2}$ W^{-1} at 1 μm) ends of the spectrum. As a result, the detectivity averaged over the entire spectral window of 350–1100 nm is also high, 1.16×10^{12} cm $Hz^{1/2}$ W^{-1}. This is ~20 times higher than for previously reported PbS NQD photodiodes.[9] The peak detectivity value of device 2 (~1.27×10^{12} cm $Hz^{1/2}$ W^{-1} at 400 nm) is close to that of device 1, however, the response is less spectrally uniform and quickly falls on the red-IR side of the spectrum. In addition to high detectivity, our devices show good linearity as illustrated in Figure 4c for light intensities spanning three orders of magnitude.

An important characteristic of a photodiode is its response time. To characterize the speed of our devices, we excite them with 100 fs, 800 nm pulses from a femtosecond laser operating at 1 kHz repetition rate. The resulting response of device 1 is displayed in Figure 4d. It shows a fairly short ~100 ns build-up time and a longer tail characterized by a few μs time constant. The temporal response of photodetectors is defined by characteristic times of carrier drift and diffusion as well as the resistance-capacitance (rC) time constant of the circuit (t_{rC}). Based on capacitance measurements, the device shown in Figure 4d has C of 3.1 nF at $V = –1.5$ V. Multiplying this value by $r = 50$ Ohm, we obtain t_{rC} of ~150 ns. This value

is close to the signal rise time in Figure 4d (~100 ns), therefore, signal buildup in these structures is likely limited by the rC time constant.

The longer constant of signal decay is indicative of an additional contribution from the charge transport time. Since in our devices the thickness of the active NQD layer is comparable to the measured depletion width, charge transport in them is primarily due to drift. The corresponding transport time, t_{dr}, can be found from $t_{dr} = W^2/\mu(\varphi + V)$, where μ is the carrier drift mobility. This expression indicates that if the width of the depletion layer does not change considerably with applied voltage (i.e., the devices are nearly depleted at $V = 0$), t_{dr} should decrease as V is increased. This trend is indeed indicated by the measurements in Figure 4d according to which the photocurrent decay time decreases from ~8 to ~4.6 μs as V changes from 0 to 1.5 V. Assuming that at $V = -1.5$ V our devices are fully depleted, and hence $W \approx d = 150$ nm (d is the NQD layer thickness), and using $\phi = 0.5$ V (derived from capacitance measurements; Figure 1c) we estimate the drift mobility of 2.5×10^{-5} cm^2 V^{-1} s^{-1}. This relatively low value suggests that while EDT treatment does improve mobility compared to films fabricated from nanocrystals with native oleic acid capping, charge transport in these structures still remains fairly inefficient. Recent studies indicate that a significant orders-of-magnitude improvement in carrier transport characteristics of NQD films can be obtained using inorganic capping strategies.[20] Such strategies are also expected to help improve the speed of nanocrystal-based devices.

3. Conclusion

To summarize, we have developed and characterized p–n junction photodiodes that utilize wide bandgap oxides as an n-type material and PbS NQDs as a p-type photoactive material. We have tested two device architectures in which either the NQD or the oxide layer is adjacent to the transparent ITO electrode. By introducing the oxide layer, we have reduced dark current under reverse bias by almost two orders of magnitude compared to earlier Schottky junction based devices. This reduction is achieved without reducing EQE, which reaches the values of ~80%. The improvement in the device architecture allows us to significantly reduce noise and obtain high detectivity of up to $>10^{12}$ cm Hz$^{1/2}$ W^{-1} extending over a broad spectral range past 1 μm. The temporal response of our devices is on the μs time scale and is limited by carrier drift within the depletion layer. We observe a sharp increase in EQE at reverse biases greater than 1 V, which we attribute to the "turn-on" of the electron contribution to the photocurrent. This contribution is small at low voltages because of short electron lifetimes. However, it increases with increasing reverse bias as the electron drift time shortens and becomes comparable to the charge transport time. Based on the change in the spectral shape of the photoresponse, which accompanies the increase in EQE, we conclude that the electrons are excited to the conduction band not from the valence band but from the occupied band of mid-gap states. This excitation mechanism does not produce mobile holes, which results in a peculiar regime of photoconduction dominated by electrons.

4. Experimental Section

Synthesis of NQDs: We synthesize PbS NQDs using lead oleate and bis(trimethylsilyl) sulfide (TMS) as precursors.[21,22] The ratio of Pb to S precursor was chosen 2:1. In a typical reaction, 0.45 g of PbO, 1.5 mL of oleic acid, and 16.5 mL of octadecene (ODE) were mixed and heated to 90 °C for 6 hours under vacuum, which produced a clear solution of lead oleate. Then the temperature of the solution was increased to 120 °C under Ar flow and 210 μL of bis(trimethylsilyl) sulfide mixed with 10 mL of ODE were swiftly injected into the reaction flask. This mixture reacted with lead oleate to produce PbS NQDs. The solution of PbS NQDs was slowly cooled and washed twice by suspending in toluene and precipitating with acetone. To replace the native oleic acid ligands for oleylamine molecules, 1 mL of oleylamine (preheated at 80 °C under vacuum) was added to the NQDs and the mixture was incubated for 2 days in a glove box.[21,22] Then, the NQDs were precipitated with acetone and redispersed in toluene. This ligand-exchange procedure was repeated three times. In the final step, NQDs were dispersed in octane at the concentration of 10 mg/ml. The synthesized nanocrystals had an average diameter of 4 nm and a bandgap of 1.18 eV as inferred from the position of the lowest energy excitonic feature in the absorption spectrum.[16]

Device Fabrication: We fabricated both types of photodiodes by a solution-based process except for the top electrode, which was made by thermal evaporation. In device 1, PEDOT:PSS (30 nm) was spin coated onto a patterned ITO coated glass substrate and subsequently annealed at 130 °C for 5 minute. The PbS NQD film was fabricated in air using a layer-by-layer deposition technique based on spin coating. Briefly, we first prepared ethanedithiol (EDT) in acetonitrile solution (1% by volume). For all spin coating steps the rotation speed was set to 2500 rpm. Each iteration of the layer-by-layer deposition consisted of two steps: (1) 1 drop of the 10 mg/mL PbS NQD octane solution was followed by (2) 1 drop of the 1% EDT solution. During step 2, oleylamine ligands were replaced for EDT.[21] This cycle was repeated twenty times. The resulting thickness of the PbS NQD film was 150 ± 10 nm. Following spin coating, the ITO/PEDOT/PbS NQD film was annealed at 90 °C for 5 min in open air. As indicated by previous studies, this procedure results in the p-type NQD layer.[21]

To fabricate a p–n junction, we deposited the n-type layer of ZnO nanoparticles (MKnano, MKN-ZnO-D40-040, ~40 nm particle size) by spin coating at 2500 rpm. The whole structure was annealed at 200 °C for 10 min under high vacuum (~1×10^{-6} mBar) in Ar atmosphere. Finally, the aluminum electrode (100 nm thickness) was thermally deposited using a shadow mask.

In the case of device 2, a TiO_2 sol–gel precursor (DuPont tyzor BTP) was diluted to 5 wt% in butanol for spin-coating.[23] The spin casted film (2500 rpm, 1 min) was subsequently annealed at 350 °C for 30 min, which formed a compact, 100 ± 10 nm thick TiO_2 film. The PbS NQD layer was fabricated using the same approach as in the case of device 1. The resulting structure was annealed at 200 °C under high vacuum. The device was completed with a top gold electrode. In the fabrication of both device 1 and device 2, we used the same patterned ITO substrates and the same shadow masks. The area of fabricated devices was 3 mm by 3 mm. The thicknesses of the PEDOT:PSS, PbS NQD, ZnO, and TiO_2 were measured using cross-sectional scanning electron microscopy (see, e.g., inset of Figure 1c).

EQE Measurements: Devices were illuminated from the ITO side using a xenon lamp as a light source. The light intensity was measured using a calibrated Si photodetector placed at the position of the tested device. In the EQE measurements, the incident light was chopped at 100 Hz.

Noise Measurements: The dark current noise under reverse bias was measured with a spectrum analyzer (Stanford Research SR760) coupled to a current preamplifier (Stanford Research SR570) in the frequency range of 1 Hz to 1.5 kHz. The devices were biased using alkaline batteries and were electrically shielded and optically sealed. During the measurements they were mounted on the optical table to reduce vibrational noise.

Acknowledgements

This material is based upon work within the Center for Advanced Solar Photophysics, an Energy Frontier Research Center funded by the U.S. Department of Energy (DOE), Office of Science, Office of Basic Energy Sciences (BES). The EQE measurements were performed at the Center for Integrated Nanotechnologies, a user facility of U.S. DOE/BES.

Received: October 20, 2011
Published online: February 13, 2012

[1] J. B. D. Soole, H. Schumacher, *IEEE J. Quantum Electron.* **1991**, *27*, 737.
[2] S. Kim, Y. T. Lim, E. G. Soltesz, A. M. De Grand, J. Lee, A. Nakayama, J. A. Parker, T. Mihaljevic, R. G. Laurence, D. M. Dor, L. H. Cohn, M. G. Bawendi, J. V. Frangioni, *Nat. Biotechnol.* **2004**, *22*, 93.
[3] A. Rogalski, J. Antoszewski, L. Faraone, *J. Appl. Phys.* **2009**, *105*, 091101.
[4] T. Rauch, M. Boberl, S. F. Tedde, J. Furst, M. V. Kovalenko, G. Hesser, U. Lemmer, W. Heiss, O. Hayden, *Nat. Photonics* **2009**, *3*, 332.
[5] M. J. Panzer, V. Wood, S. M. Geyer, M. G. Bawendi, V. Bulovic, *J. Display Technol.* **2010**, *6*, 90.
[6] X. Geng, L. Niu, Z. Xing, R. Song, G. Liu, M. Sun, G. Cheng, H. Zhong, Z. Liu, Z. Zhang, L. Sun, H. Xu, L. Lu, L. Liu, *Adv. Mater.* **2010**, *22*, 638.
[7] V. Wood, M. J. Panzer, J. Chen, M. S. Bradley, J. E. Halpert, M. G. Bawendi, V. Bulović, *Adv. Mater.* **2009**, *21*, 2151.
[8] S. A. McDonald, G. Konstantatos, S. Zhang, P. W. Cyr, E. J. D. Klem, L. Levina, E. H. Sargent, *Nat. Mater.* **2005**, *4*, 138.
[9] J. P. Clifford, G. Konstantatos, K. W. Johnston, S. Hoogland, L. Levina, E. H. Sargent, *Nat. Nanotechnol.* **2009**, *4*, 40.
[10] G. Sarasqueta, K. R. Choudhury, F. So, *Chem. Mater.* **2010**, *22*, 3496.
[11] S. Hinds, L. Levina, E. J. D. Klem, G. Konstantatos, V. Sukhovatkin, E. H. Sargent, *Adv. Mater.* **2008**, *20*, 4398.
[12] G. Konstantatos, L. Levina, J. Tang, E. H. Sargent, *Nano Lett.* **2008**, *8*, 4002.
[13] G. Konstantatos, I. Howard, A. Fischer, S. Hoogland, J. Clifford, E. Klem, L. Levina, E. H. Sargent, *Nature* **2006**, *442*, 180.
[14] S. M. Sze, K. K. Ng, *Physics of Semiconductor Devices* 3rd. ed., John Wiley & Sons, New Jersey **2007**, Ch. 13.
[15] P. R. Brown, R. R. Lunt, N. Zhao, T. P. Osedach, D. D. Wanger, L.-Y. Chang, M. G. Bawendi, V. Bulović, *Nano Lett.* **2011**, *11*, 2955.
[16] J. Gao, J. M. Luther, O. E. Semonin, R. J. Ellingson, A. J. Nozik, M. C. Beard, *Nano Lett.* **2011**, *11*, 1002.
[17] J. Tang, E. H. Sargent, *Adv. Mater.* **2011**, *23*, 12.
[18] L. Ching-Ting, L. Tzu-Shun, L. Hsin-Ying, *IEEE Photon. Technol. Lett.* **2010**, *22*, 1117.
[19] P. Nagpal, V. I. Klimov, *Nat. Commun.* **2011**, *2*, 486.
[20] M. V. Kovalenko, M. Scheele, D. V. Talapin, *Science* **2009**, *324*, 1417.
[21] J. Tang, L. Brzozowski, D. A. R. Barkhouse, X. Wang, R. Debnath, R. Wolowiec, E. Palmiano, L. Levina, A. G. Pattantyus-Abraham, D. Jamakosmanovic, E. H. Sargent, *ACS Nano* **2010**, *4*, 869.
[22] J. Tang, X. Wang, L. Brzozowski, D. A. R. Barkhouse, R. Debnath, L. Levina, E. H. Sargent, *Adv. Mater.* **2010**, *22*, 1398.
[23] K.-S. Cho, E. K. Lee, W.-J. Joo, E. Jang, T.-H. Kim, S. J. Lee, S.-J. Kwon, J. Y. Han, B.-K. Kim, B. L. Choi, J. M. Kim, *Nat. Photonics* **2009**, *3*, 341.